

Dissipation and Interaction-Controlled Non-Hermitian Skin Effects

Yang Li,^{1,*} Zhao-Fan Cai,^{1,*} Tao Liu,^{1,†} and Franco Nori^{2,3,4}

¹*School of Physics and Optoelectronics, South China University of Technology, Guangzhou 510640, China*

²*Theoretical Quantum Physics Laboratory, Cluster for Pioneering Research, RIKEN, Wako-shi, Saitama 351-0198, Japan*

³*RIKEN Center for Quantum Computing, Wako-shi, Saitama 351-0198, Japan*

⁴*Department of Physics, University of Michigan, Ann Arbor, Michigan 48109-1040, USA*

(Dated: August 27, 2024)

Non-Hermitian skin effects (NHSEs) have recently been investigated extensively at the single-particle level. When many-body interactions become dominant, novel non-Hermitian physical phenomena can emerge. In this work, we theoretically study NHSEs controlled by dissipation and interaction. We consider a 1D zigzag Bose-Hubbard lattice, subject to magnetic flux, staggered onsite single-particle loss, and uniform onsite two-particle loss. When the two-particle loss is small, two-body bound eigenstates (i.e., doublons) are all localized at the same boundary due to the interplay of the magnetic flux and staggered single-particle loss. While, for strong two-particle loss, the localization direction of doublons is unexpectedly reversed. This is attributed to the effective strong nonreciprocal hopping of doublons contributing from the virtual second-order and third-order hopping processes of particle pairs in combination with the magnetic flux, the strong two-particle loss, and the many-body interaction. Moreover, a two-particle gain can induce the same skin-localization of doublons, which can be utilized to dynamically observe the NHSE and its reversal of doublons controlled by interactions. Our results open up a new avenue for exploring novel non-Hermitian phenomena in many-body systems.

Introduction.—In the framework of non-Hermitian quantum mechanics [1], open quantum systems described by effective non-Hermitian Hamiltonians exhibit many striking physical phenomenon without Hermitian counterparts [2–48]. One of the fascinating properties of non-Hermitian systems is the localization of bulk modes at the boundaries [9–17], dubbed the non-Hermitian skin effect (NHSE). The NHSE originates from the intrinsic point-gap topology of complex eigenenergies [27]. Recently, many efforts have been devoted to exploring unique consequences of NHSE without many-body interactions, e.g., breakdown of conventional Bloch band theory [9–11] and entanglement phase transitions [34].

When many-body interactions are introduced into non-Hermitian systems, unusual physical properties can emerge [49–70]. Especially, with nonreciprocal hopping, many-body interactions have the potential to induce NHSE [60], occupation-dependent NHSE [64], non-Hermitian Mott skin effect [65], dynamical suppression of NHSE [66], and so on. However, it is challenging to implement the nonreciprocal hopping in order to achieve the NHSE for many experimental platforms. A more operational approach is to utilize onsite loss or gain [30, 43, 71–73]. Therefore, a natural open question arises: can the onsite loss or gain be utilized to induce and even control NHSEs in the interacting non-Hermitian system?

In this work, we study the NHSE in dissipative and interacting systems without nonreciprocal hopping. Specifically, we consider a 1D zigzag Bose-Hubbard lattice in the presence of a magnetic flux piercing through each triangular plaquette. By introducing the imbalanced onsite single-particle loss at the odd and even sites and uniform onsite two-particle loss, two branches of doublon (i.e., a bound pair at the same site) bands form.

For weak two-particle loss, the states from two doublon bands are all localized at the same boundary due to the interplay of the magnetic-flux-induced chiral transport and staggered single-particle loss. Most remarkably, the states from one branch of the doublon bands are unexpectedly reversely localized at the other boundary for strong two-particle loss. The underlying hidden physical mechanism is revealed: there is an effectively strong nonreciprocal hopping contributing from the virtual second-order and third-order hopping processes of particle pairs in combination with the magnetic flux, the strong two-particle loss, and the interaction. We finally discuss the same reversal of the NHSE induced by adding two-particle gain. Moreover, with two-particle gain, the initial two-particle excitation can remain strongly bound during the dynamical evolution, which can be utilized to observe dynamical NHSE and its reversal of doublons controlled by the interactions.

Model.—We consider a 1D zigzag bosonic chain in the presence of onsite many-body interactions, single-particle and two-particle dissipation, as shown in Fig. 1. In addition, a synthetic magnetic flux ϕ piercing through each triangular plaquette is introduced. The Bose-Hubbard Hamiltonian is written as

$$\hat{\mathcal{H}} = - \sum_{j=1}^{L/2-1} \left(t' e^{i\phi} \hat{a}_{2j+2}^\dagger \hat{a}_{2j} + t' e^{-i\phi} \hat{a}_{2j+1}^\dagger \hat{a}_{2j-1} + \text{H.c.} \right) - \sum_{j=1}^{L-1} t \left(\hat{a}_{j+1}^\dagger \hat{a}_j + \text{H.c.} \right) - U \sum_{j=1}^L \hat{a}_j^\dagger \hat{a}_j^\dagger \hat{a}_j \hat{a}_j, \quad (1)$$

where \hat{a}_j annihilates a boson at site j , t and t' represent the nearest-neighbor and next-nearest-neighbor hopping strengths, U denotes the many-body interacting

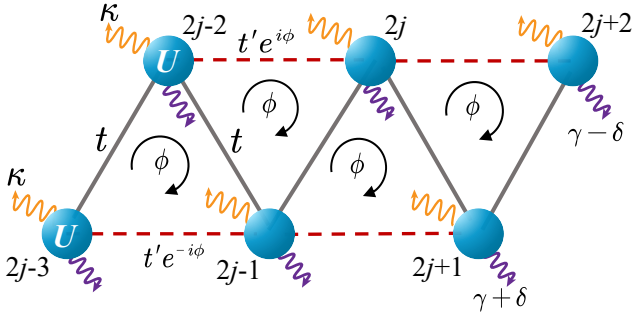


FIG. 1. Schematic showing a two-leg zigzag chain in the presence of onsite interaction U , imbalanced onsite single-particle loss (denoted by purple wavy lines) with decay rate $\gamma \pm \delta$ on two legs, and uniform onsite two-particle loss (denoted by yellow wavy lines) with decay rate κ . A synthetic magnetic flux ϕ piercing through each triangular plaquette is introduced. The black solid and red dashed lines represent the nearest-neighbor and next-nearest-neighbor hopping with strengths t and t' .

strength, and L is the number of lattice sites.

We suppose that the lattice undergoes the imbalanced onsite single-particle loss $\gamma \pm \delta$ between two legs, and uniform onsite two-particle loss κ (see Fig. 1). The system dynamics is governed by the Lindblad master equation [74–76]

$$\begin{aligned} \frac{d\hat{\rho}}{dt} = & -i [\hat{\mathcal{H}}, \hat{\rho}] + \sum_j [\gamma - (-1)^j \delta] \mathcal{D}[\hat{a}_j] \hat{\rho} \\ & + \sum_j \kappa \mathcal{D}[\hat{a}_j \hat{a}_j] \hat{\rho}, \end{aligned} \quad (2)$$

where $\hat{\rho}$ is the system density matrix, and the Lindblad superoperator $\mathcal{D}[\hat{\mathcal{L}}] \hat{\rho} = \hat{\mathcal{L}} \hat{\rho} \hat{\mathcal{L}}^\dagger - \{\hat{\mathcal{L}}^\dagger \hat{\mathcal{L}}, \hat{\rho}\}/2$ represents bosonic dissipation.

By continuously monitoring particle number [77], the dissipative system in Eq. (2) is described by the non-Hermitian Hamiltonian

$$\hat{\mathcal{H}}_{\text{NH}} = \hat{\mathcal{H}} - i \frac{\kappa}{2} \sum_{j=1}^L \hat{a}_j^\dagger \hat{a}_j^\dagger \hat{a}_j \hat{a}_j - \frac{i}{2} \sum_{j=1}^L [\gamma - (-1)^j \delta] \hat{n}_j, \quad (3)$$

where $\hat{n}_j = \hat{a}_j^\dagger \hat{a}_j$ is density operator. Due to $[\hat{\mathcal{H}}_{\text{NH}}, \sum_j \hat{n}_j] = 0$, we can study the arbitrary subspace of the particle number in the Fock basis. Here, we consider the double-excitation subspace and assume $\phi = \pi/2$.

Single-Particle Dissipation Induced NHSE.—We first study the NHSE in the presence of only the single-particle dissipation with $\kappa = 0$. We plot the complex eigenenergies of $\hat{\mathcal{H}}_{\text{NH}}$ under open boundary conditions (OBCs, blue dots) and periodic boundary conditions (PBCs, red dots) in Fig. 2(a). The eigenspectrum is divided into continuous scattering states and discrete

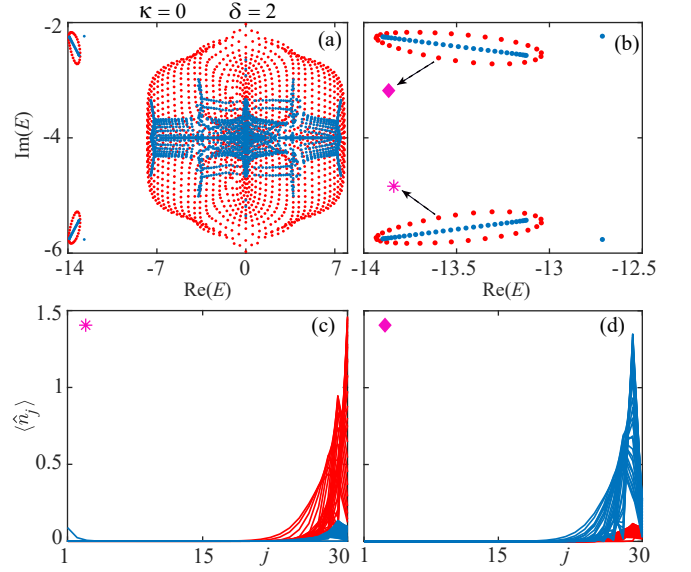


FIG. 2. (a) Complex eigenenergies of $\hat{\mathcal{H}}_{\text{NH}}$ under OBCs (blue dots) and PBCs (red dots) for $\kappa = 0$ and $\delta = 2$. The zoom-in view of the two doubton bands on the far left of (a) is shown in (b), where the magenta star and diamond denote the two branches of the doubton bands. The corresponding particle densities $\langle \hat{n}_j \rangle$ are shown in (c) and (d) under OBCs, where the red (blue) curves indicate the state distributions at the odd (even) sites. Other parameters are: $U = 6$, $t = 2$, $t' = 1$, $\gamma = 4$, $\delta = 2$, and $L = 60$.

doubton bands. The scattering states consist of superpositions of two-particle states residing on different sites, while the doubton bands are composed of bound-particle pairs residing on the same site, with their eigenenergies well separated from the continuum of scattering states [see Fig. 2(a)]. In this work, we focus on two doubton bands, of which the zoom-in view on the far left of Fig. 2(a) is shown in Fig. 2(b). In the complex plane, each doubton band, indicated by the magenta star and diamond, forms a point gap (red dots) under PBCs. Each of these point gaps encircles the respective doubton band (blue dots) under OBCs, indicating usually the occurrence of NHSE. In order to demonstrate this indeed the case, we calculate the particle density as

$$\langle \hat{n}_j \rangle = \frac{{}_R \langle \psi_m | \hat{n}_j | \psi_m \rangle_R}{{}_R \langle \psi_m | \psi_m \rangle_R}, \quad (4)$$

where $|\psi_m\rangle_R$ ($m = 1, 2, 3, \dots$) is the m th right eigenvector with $\hat{\mathcal{H}}_{\text{NH}} |\psi_m\rangle_R = E_m |\psi_m\rangle_R$.

The site-resolved particle densities of two doubton bands are shown in Figs. 2(c,d), respectively, where red (blue) curves indicate state distributions at odd (even) sites. All the doublons are localized at the right boundary, indicating the NHSE. Moreover, the states from two branches of doubton bands occupy different legs of the zigzag lattice, where the states from the doubton band with larger (smaller) loss reside mainly the odd

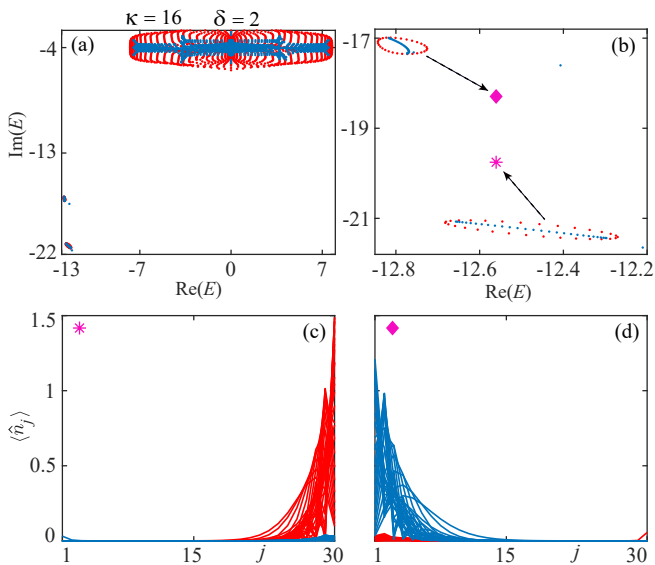


FIG. 3. Complex eigenenergies of $\hat{\mathcal{H}}_{\text{nH}}$ under OBCs (blue dots) and PBCs (red dots) for $\kappa = 16$ and $\delta = 2$. The zoom-in view of the two doublon bands on the far left of (a) is shown in (b), where the magenta star and diamond denote two branches of doublon bands. The corresponding particle densities $\langle \hat{n}_j \rangle$ are shown in (c) and (d) under OBCs, where the red (blue) curves indicate the state distributions at the odd (even) sites. Other parameters are: $U = 6$, $t = 2$, $t' = 1$, $\gamma = 4$, and $L = 60$.

(even) sites [see Fig. 2(c,d)]. For the single-particle loss, the NHSE of doublons is attributed to the interplay of the effective magnetic flux of doublons, and the renormalized imbalanced loss between its two legs (see the effective Hamiltonian of doublons in Supplementary Materials (SM) in Ref. [78]). The non-zero flux leads to opposite particle transports along the two legs [30, 79]. Due to the larger loss at the odd sites, the particle transport towards the right boundary are favored, and the backflow is suppressed. This leads to the skin-mode localization at the right boundary. Note that two isolated states of doublons, lying outside the point gaps [Fig. 2(b)], are localized at either the left or right boundary. There are two-particle Tamm-Shockley edge states [80, 81], resulting from different effective onsite potential at the edges and bulk (see details in Ref. [78]), which have no topological origin.

The NHSE originates from intrinsic non-Hermitian topology. In order to characterize the point-gap topology, we introduce a twist angle φ ($\varphi \in [0, 2\pi]$) to PBC, and define the many-body winding number [54, 56, 58]

$$\mathcal{W} = \oint_0^{2\pi} \frac{d\varphi}{2\pi i} \frac{\partial}{\partial \varphi} \log \left[\det \left(\hat{\mathcal{H}}_{\text{nH}} - E_{\text{ref}} \right) \right], \quad (5)$$

where E_{ref} is the complex reference energy inside the point gap. The nonzero winding number with $\mathcal{W} = 2$ for each doublon band indicates the intrinsic topological origin of doublons' NHSE.

Two-Particle Dissipation Controlled NHSE.—We include the effects of the strong two-particle loss with $\kappa = 16$ and $\delta = 2$, and plot the complex eigenenergies of $\hat{\mathcal{H}}_{\text{nH}}$ under OBCs (blue dots) and PBCs (red dots) in Fig. 3(a). The zoom-in view of the doublon bands is shown in Fig. 3(b). The eigenenergies of OBCs are enclosed by the point-gap loop, indicating the appearance of NHSE. In contrast to the case of single-particle dissipation, the two-particle loss reverses the localization direction of doublons, as shown in Fig. 3(c,d). The states from the doublon band with the larger loss occupy the odd sites and are still localized at the right boundary [see Fig. 3(c)]. However, the states from the other doublon band with the smaller loss are unexpectedly localized at the left boundary [see Fig. 3(d)], where they occupy the even sites. In addition, the winding number of the doublon band with the smaller loss becomes $\mathcal{W} = -2$, indicating also the reversal of NHSE. Furthermore, the localization direction of the doublons can be tuned by the interaction, single-particle loss or two-particle dissipation. For instance, by fixing the two-particle loss κ , but increasing the single-particle dissipation δ , we observe once more the reversal of the localization direction of the doublon band [78].

In order to understand the underlying hidden mechanism of the unexpected reversal of the localization direction of the doublons, we derive the effective Hamiltonian $\hat{\mathcal{H}}_{\text{eff}}$ describing the doublon bands in the strong-interaction limit with $U \gg t, t'$. In this case, the doublons are tightly bound, and their bands are energetically well-separated from two-particle scattering states. Therefore, we can split the Hamiltonian $\hat{\mathcal{H}}_{\text{nH}}$ into its dominant term, with $\hat{\mathcal{H}}_0 = -(U + i\kappa/2) \sum_j \hat{n}_j (\hat{n}_j - 1) - \frac{i}{2} \sum_j [\gamma - (-1)^j \delta] \hat{n}_j$, and treat the remaining terms as the perturbation. Based on third-order quasidegenerate perturbation theory [78], we obtain the effective Hamiltonian $\hat{\mathcal{H}}_{\text{eff}}$ of doublons as

$$\begin{aligned} \hat{\mathcal{H}}_{\text{eff}} = & -t_0 \sum_j \left(\hat{d}_{j+1}^\dagger \hat{d}_j + \text{H.c.} \right) + \sum_j \left(U_1 \hat{n}_{2j-1} + U_2 \hat{n}_{2j} \right) \\ & - \sum_j \left(J_{1,R} \hat{d}_{2j+1}^\dagger \hat{d}_{2j-1} + J_{1,L} \hat{d}_{2j-1}^\dagger \hat{d}_{2j+1} \right) \\ & - \sum_j \left(J_{2,R} \hat{d}_{2j+2}^\dagger \hat{d}_{2j} + J_{2,L} \hat{d}_{2j}^\dagger \hat{d}_{2j+2} \right), \quad (6) \end{aligned}$$

where $J_{1,R} = J(\delta, \phi)$, $J_{1,L} = J(\delta, -\phi)$, $J_{2,R} = J(-\delta, -\phi)$, $J_{2,L} = J(-\delta, \phi)$, $U_1 = U(\delta)$, $U_2 = U(-\delta)$, and

$$\begin{aligned} t_0 = & \left[\frac{2U}{4U^2 + (\kappa + \delta)^2} + \frac{2U}{4U^2 + (\kappa - \delta)^2} \right] t^2 \\ & - i \left(\frac{\kappa + \delta}{4U^2 + (\kappa + \delta)^2} + \frac{\kappa - \delta}{4U^2 + (\kappa - \delta)^2} \right) t^2, \quad (7) \end{aligned}$$

$$J(\delta, \phi) = \frac{4t^2 t'}{(2U + i\kappa)(2U + i\kappa + i\delta)} e^{-i\phi} + \frac{2t^2 t'}{(2U + i\kappa + i\delta)^2} e^{-i\phi} + \frac{2t'^2}{2U + i\kappa} e^{-2i\phi}, \quad (8)$$

$$U(\delta) = - \left[2U + \frac{8Ut^2}{4U^2 + (\kappa + \delta)^2} + \frac{8Ut'^2}{4U^2 + \kappa^2} \right] + i \left[\frac{4(\kappa + \delta)t^2}{4U^2 + (\kappa + \delta)^2} + \frac{4\kappa t'^2}{4U^2 + \kappa^2} - \kappa - \gamma - \delta \right]. \quad (9)$$

As shown by the above effective Hamiltonian, the zigzag lattice of doublons is pierced through the magnetic flux [see Eq. (8)], where there exists the imbalanced complex onsite potential $U(\pm\delta)$ along two legs [see Eq. (9)]. Most remarkably, along each leg of the lattice, the virtual second-order hopping process of particle pairs contributes to an effective phase 2ϕ , and third-order process contributes to ϕ in Eq. (8) (see details in Ref. [78]). Therefore, *the effective next-nearest neighbor hopping of doublons becomes nonreciprocal*, i.e., $|J_{i,R}| \neq |J_{i,L}|$ ($i = 1, 2$) in Eq. (8), *due to the interplay of the strong two-particle dissipation and the magnetic flux in the presence of the many-body interactions*. Moreover, the nonreciprocal-hopping direction can be different along two legs, determined by the interaction U , two-particle loss κ , and imbalanced single-particle loss δ .

As discussed above, with the two-particle loss, the skin-mode localization direction of doublons is determined by the competition between the effective nonreciprocal hopping, induced by the two-particle dissipation and magnetic flux, and the directional hopping due to the interplay of magnetic-flux induced chiral transport and imbalanced loss along two legs. This contrasts with the single-particle case, where the NHSE results from the interplay of the magnetic-flux-induced chiral transport and the imbalanced onsite loss along two legs of the zigzag lattice structure in Fig. 1. By fixing $U = 6$ and $\delta = 2$, we have $|J_{1,R}| > |J_{1,L}|$ and $|J_{2,R}| < |J_{2,L}|$ for $\kappa > \delta$. If the two-particle dissipation κ is comparable with the interaction strength U , all the states from two doublon bands are localized at the right boundary (see discussions with $\kappa = 7$ in Ref. [78]). This is mainly attributed to the directional hopping due to the interplay of the magnetic-flux-induced chiral transport and imbalanced loss along two legs of doublons [see Eqs. (8, 9)] in spite of the slightly larger hopping strength towards the left boundary along the even sites. However, as the two-particle dissipation strength κ is further increased, the asymmetrical hopping towards the left boundary becomes much stronger than hopping towards the right one along the even sites. This finally reverses the localization direction of the states from the doublon band with the smaller loss for $\kappa \gg U$, where they are localized at the left boundary along the even sites [see Fig. 3(d)]. Furthermore, if δ is increased

and becomes comparable with κ , we have $|J_{1,R}| > |J_{1,L}|$ and $|J_{2,R}| > |J_{2,L}|$. This causes once more the reversal of NHSE along the even sites [see Fig. 3(h)].

Two-Particle Pumping and Dynamics.—We now proceed to study the evolution dynamics of doublons. When the system is subjected to both single-particle and two-particle dissipation, the state decays during the dynamical evolution, and collapses into the system's eigenstate with the largest imaginary part of its eigenenergy after a long-time evolution. For the double-excitation subspace, the eigenenergies of scattering states have the larger imaginary parts than those of doublons (see Fig. 3). Therefore, the system eventually evolves into the scattering state in spite of the initial doublon excitation, leading to the doublon dissociation [62].

According to the above effective Hamiltonian of doublons in the strong-interaction limit, we infer that the two-particle gain with $\kappa < 0$ plays the same role in determining the localization direction of doublons as the two-particle loss with $\kappa > 0$. Therefore, in order to dynamically observe the NHSE reversal of doublons controlled by the interaction, we study the NHSE by introducing the two-particle gain along the odd sites via incoherent two-particle pumping. The effective non-Hermitian Hamiltonian becomes

$$\hat{\mathcal{H}}_{\text{nHG}} = \hat{\mathcal{H}} - i \frac{\kappa}{2} \sum_{j=1}^{L/2} \hat{a}_{2j-1}^\dagger \hat{a}_{2j-1}^\dagger \hat{a}_{2j-1} \hat{a}_{2j-1} - \frac{i}{2} \sum_{j=1}^L [\gamma - (-1)^j \delta] \hat{n}_j, \quad (10)$$

where $\kappa < 0$. By setting $U = 0.5$, $\gamma = 1$ and $\delta = 0.5$, all the doublons are localized at the right boundary for small two-particle gain with $\kappa = -0.5$ (see Fig. 4(a-c) and also Ref. [78]) due to the interplay of the magnetic-flux-induced chiral transport and the larger onsite loss along the odd sites. For the large two-particle gain with $\kappa = -2$, the effective loss (it is equivalent to add a large background loss) at odd sites becomes smaller than that at even sites. However, not all the doublon states are localized towards the left boundary, and the states from one doublon band are still unexpectedly localized at the right boundary along the even sites [see Fig. 4(e-g)].

The dynamical evolution of the system is calculated according to

$$|\psi(t)\rangle = \frac{e^{-i\hat{\mathcal{H}}_{\text{nHG}}t} |\psi_0\rangle}{\langle \psi_0 | e^{i\hat{\mathcal{H}}_{\text{nHG}}^\dagger t} e^{-i\hat{\mathcal{H}}_{\text{nHG}}t} | \psi_0 \rangle}, \quad (11)$$

where the initial state is chosen as the double-occupied state (i.e., a doublon) at the site j with $|\psi_0\rangle = 1/\sqrt{2} \hat{a}_j^\dagger \hat{a}_j^\dagger |0\rangle$. Then, we calculate the time-resolved doublon density $\langle \hat{n}_j^d \rangle = \langle \psi(t) | \hat{a}_j^\dagger \hat{a}_j^\dagger \hat{a}_j \hat{a}_j | \psi(t) \rangle / 2$.

As shown in Fig. 4(d,h), with the two-particle gain κ , the onsite two-particle excitation is strongly bound

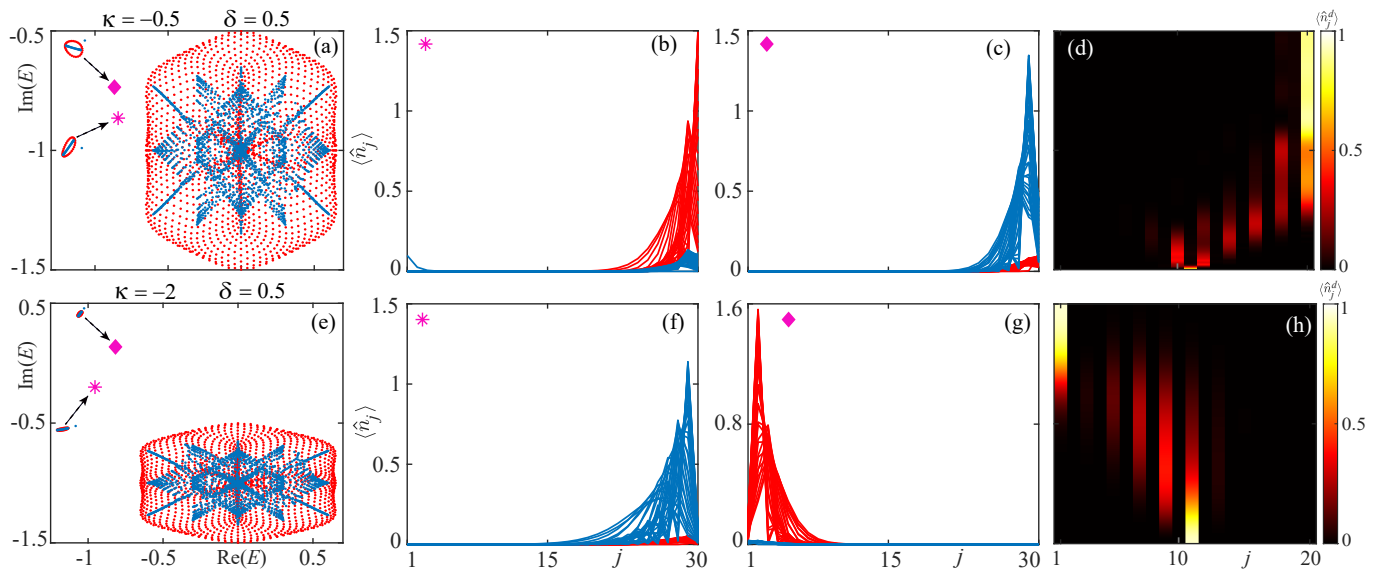


FIG. 4. Complex eigenenergies of \hat{H}_{NHG} under OBCs (blue dots) and PBCs (red dots) subject to the two-particle gain (a) for $\kappa = -0.5$ and (e) for $\kappa = -2$. The magenta star and diamond denote the two doublon bands on the far left of both (a) and (e). The corresponding particle densities $\langle \hat{n}_j \rangle$ are shown in (b,c) and (f,g) under OBCs, where the red (blue) curves indicate state distributions at the odd (even) sites. Evolution dynamics of the doublon density $\langle \hat{n}_j^d \rangle$ with a double-occupied state initially prepared at the odd site (d) for $\kappa = -0.5$, and (h) for $\kappa = -2$. Other parameters are: $U = 0.5$, $t = 0.2$, $t' = 0.1$, $\gamma = 1$, and $\delta = 0.5$.

during the dynamical evolution for the double-occupied state initially prepared at the odd site. For small $|\kappa|$ with $\kappa = -0.5$, as expected, the doublon transports towards the right boundary [see Fig. 4(d)]. While, for the large two-particle gain with $\kappa = -2$, the evolution direction is reversed [see Fig. 4(h)], indicating the reversal of NHSE controlled by the two-particle gain.

Conclusion.—We investigate the loss or gain controlled NHSEs, with the combination of the Bose-Hubbard interaction, in a 1D zigzag lattice subject to a magnetic flux threading through each triangular plaquette. By introducing imbalanced onsite single-particle loss on the odd and even sites, we realize all the states, from two doublon bands, localized at the same boundary due to the interplay of the magnetic-flux-induced chiral transport and staggered single-particle loss. Imposing the uniform onsite two-particle loss or gain produces an unexpected reversal of the localization direction of one doublon band. This results from the effectively strong nonreciprocal hopping contributing from the virtual second-order and third-order hopping processes of particle pairs. In experiments, our predictions could be tested experimentally using ultracold atoms [33, 73, 79], and simulated in the electrical circuits by mapping the 1D two-particle excitation into a 2D lattice [82]. In the future, it is interesting to explore the NHSEs controlled by interaction and loss beyond double-excitation subspace.

T.L. acknowledges the support from National Natural Science Foundation of China (Grant No. 12274142),

Introduced Innovative Team Project of Guangdong Pearl River Talents Program (Grant No. 2021ZT09Z109), the Fundamental Research Funds for the Central Universities (Grant No. 2023ZYGXZR020), and the Startup Grant of South China University of Technology (Grant No. 20210012). F.N. is supported in part by: Nippon Telegraph and Telephone Corporation (NTT) Research, the Japan Science and Technology Agency (JST)[via the Quantum Leap Flagship Program (Q-LEAP), and the Moonshot R&D Grant Number JPMJMS2061], the Asian Office of Aerospace Research and Development (AOARD) (via Grant No. FA2386-20-1-4069), and the Office of Naval Research (ONR) Global (via Grant No. N62909-23-1-2074).

* These authors contributed equally

† E-mail: liutao0716@scut.edu.cn

- [1] Y. Ashida, Z. Gong, and M. Ueda, “Non-Hermitian physics,” *Adv. Phys.* **69**, 249 (2020).
- [2] B. Peng, Ş. K. Özdemir, F. Lei, F. Monifi, M. Gianfreda, G. L. Long, S. Fan, F. Nori, C. M. Bender, and L. Yang, “Parity–time-symmetric whispering-gallery microcavities,” *Nat. Phys.* **10**, 394 (2014).
- [3] B. Peng, Ş. K. Özdemir, S. Rotter, H. Yilmaz, M. Liertzer, F. Monifi, C. M. Bender, F. Nori, and L. Yang, “Loss-induced suppression and revival of lasing,” *Science* **346**, 328 (2014).
- [4] T. Gao, E. Estrecho, K. Y. Bliokh, T. C. H. Liew, M. D. Fraser, S. Brodbeck, M. Kamp, C. Schneider, S. Höfling,

- Y. Yamamoto, F. Nori, Y. S. Kivshar, A. G. Truscott, R. G. Dall, and E. A. Ostrovskaya, "Observation of non-Hermitian degeneracies in a chaotic exciton-polariton billiard," *Nature* **526**, 554 (2015).
- [5] D. Leykam, K. Y. Bliokh, C. Huang, Y. D. Chong, and F. Nori, "Edge modes, degeneracies, and topological numbers in non-Hermitian systems," *Phys. Rev. Lett.* **118**, 040401 (2017).
- [6] Y. Xu, S. T. Wang, and L. M. Duan, "Weyl exceptional rings in a three-dimensional dissipative cold atomic gas," *Phys. Rev. Lett.* **118**, 045701 (2017).
- [7] Z. Gong, Y. Ashida, K. Kawabata, K. Takasan, S. Higashikawa, and M. Ueda, "Topological phases of non-Hermitian systems," *Phys. Rev. X* **8**, 031079 (2018).
- [8] R. El-Ganainy, K. G. Makris, M. Khajavikhan, Z. H. Musslimani, S. Rotter, and D. N. Christodoulides, "Non-Hermitian physics and PT symmetry," *Nat. Phys.* **14**, 11 (2018).
- [9] S. Yao and Z. Wang, "Edge states and topological invariants of non-Hermitian systems," *Phys. Rev. Lett.* **121**, 086803 (2018).
- [10] K. Zhang, Z. Yang, and C. Fang, "Correspondence between winding numbers and skin modes in non-Hermitian systems," *Phys. Rev. Lett.* **125**, 126402 (2020).
- [11] K. Yokomizo and S. Murakami, "Non-Bloch band theory of non-Hermitian systems," *Phys. Rev. Lett.* **123**, 066404 (2019).
- [12] S. Yao, F. Song, and Z. Wang, "Non-Hermitian Chern bands," *Phys. Rev. Lett.* **121**, 136802 (2018).
- [13] F. K. Kunst, E. Edvardsson, J. C. Budich, and E. J. Bergholtz, "Biorthogonal bulk-boundary correspondence in non-Hermitian systems," *Phys. Rev. Lett.* **121**, 026808 (2018).
- [14] T. Liu, Y.-R. Zhang, Q. Ai, Z. Gong, K. Kawabata, M. Ueda, and F. Nori, "Second-order topological phases in non-Hermitian systems," *Phys. Rev. Lett.* **122**, 076801 (2019).
- [15] F. Song, S. Yao, and Z. Wang, "Non-Hermitian skin effect and chiral damping in open quantum systems," *Phys. Rev. Lett.* **123**, 170401 (2019).
- [16] J. Y. Lee, J. Ahn, H. Zhou, and A. Vishwanath, "Topological correspondence between Hermitian and non-Hermitian systems: Anomalous dynamics," *Phys. Rev. Lett.* **123**, 206404 (2019).
- [17] K. Kawabata, T. Bessho, and M. Sato, "Classification of exceptional points and non-Hermitian topological semimetals," *Phys. Rev. Lett.* **123**, 066405 (2019).
- [18] J. Zhang, B. Peng, Ş. K. Özdemir, K. Pichler, D. O. Krimer, G. Zhao, F. Nori, Y.-x. Liu, S. Rotter, and L. Yang, "A phonon laser operating at an exceptional point," *Nat. Photon.* **12**, 479 (2018).
- [19] K. Y. Bliokh, D. Leykam, M. Lein, and F. Nori, "Topological non-Hermitian origin of surface Maxwell waves," *Nat. Comm.* **10**, 580 (2019).
- [20] Z. Y. Ge, Y. R. Zhang, T. Liu, S. W. Li, H. Fan, and F. Nori, "Topological band theory for non-Hermitian systems from the Dirac equation," *Phys. Rev. B* **100**, 054105 (2019).
- [21] F. Minganti, A. Miranowicz, R. W. Chhajlany, and F. Nori, "Quantum exceptional points of non-Hermitian Hamiltonians and Liouvillians: The effects of quantum jumps," *Phys. Rev. A* **100**, 062131 (2019).
- [22] H. Zhao, X. Qiao, T. Wu, B. Midya, S. Longhi, and L. Feng, "Non-Hermitian topological light steering," *Science* **365**, 1163 (2019).
- [23] K. Kawabata, K. Shiozaki, M. Ueda, and M. Sato, "Symmetry and topology in non-Hermitian physics," *Phys. Rev. X* **9**, 041015 (2019).
- [24] D. S. Borgnia, A. J. Kruchkov, and R.-J. Slager, "Non-Hermitian boundary modes and topology," *Phys. Rev. Lett.* **124**, 056802 (2020).
- [25] F. Minganti, A. Miranowicz, R. W. Chhajlany, I. I. Arkhipov, and F. Nori, "Hybrid-Liouvillian formalism connecting exceptional points of non-Hermitian Hamiltonians and Liouvillians via postselection of quantum trajectories," *Phys. Rev. A* **101**, 062112 (2020).
- [26] I. I. Arkhipov, A. Miranowicz, F. Minganti, and F. Nori, "Liouvillian exceptional points of any order in dissipative linear bosonic systems: Coherence functions and switching between \mathcal{PT} and anti- \mathcal{PT} symmetries," *Phys. Rev. A* **102**, 033715 (2020).
- [27] N. Okuma, K. Kawabata, K. Shiozaki, and M. Sato, "Topological origin of non-Hermitian skin effects," *Phys. Rev. Lett.* **124**, 086801 (2020).
- [28] T. Liu, J. J. He, Z. Yang, and F. Nori, "Higher-order Weyl-exceptional-ring semimetals," *Phys. Rev. Lett.* **127**, 196801 (2021).
- [29] E. J. Bergholtz, J. C. Budich, and F. K. Kunst, "Exceptional topology of non-Hermitian systems," *Rev. Mod. Phys.* **93**, 015005 (2021).
- [30] Y. Li, C. Liang, C. Wang, C. Lu, and Y.-C. Liu, "Gain-loss-induced hybrid skin-topological effect," *Phys. Rev. Lett.* **128**, 223903 (2022).
- [31] K. Zhang, Z. Yang, and C. Fang, "Universal non-Hermitian skin effect in two and higher dimensions," *Nat. Commun.* **13** (2022).
- [32] K. Li and Y. Xu, "Non-Hermitian absorption spectroscopy," *Phys. Rev. Lett.* **129**, 093001 (2022).
- [33] Z. Ren, D. Liu, E. Zhao, C. He, K. K. Pak, J. Li, and G.-B. Jo, "Chiral control of quantum states in non-Hermitian spin-orbit-coupled fermions," *Nat. Phys.* **18**, 385 (2022).
- [34] K. Kawabata, T. Numasawa, and S. Ryu, "Entanglement phase transition induced by the non-Hermitian skin effect," *Phys. Rev. X* **13**, 021007 (2023).
- [35] K. Zhang, C. Fang, and Z. Yang, "Dynamical degeneracy splitting and directional invisibility in non-Hermitian systems," *Phys. Rev. Lett.* **131**, 036402 (2023).
- [36] C.-A. Li, B. Trauzettel, T. Neupert, and S.-B. Zhang, "Enhancement of second-order non-Hermitian skin effect by magnetic fields," *Phys. Rev. Lett.* **131**, 116601 (2023).
- [37] C. Leefmans, A. Dutt, J. Williams, L. Yuan, M. Parto, F. Nori, S. Fan, and A. Marandi, "Topological dissipation in a time-multiplexed photonic resonator network," *Nat. Phys.* **18**, 442 (2022).
- [38] N. Okuma and M. Sato, "Non-Hermitian topological phenomena: A review," *Annu. Rev. Condens. Matter Phys.* **14**, 83 (2023).
- [39] X. Li, J. Liu, and T. Liu, "Localization-delocalization transitions in non-Hermitian Aharonov-Bohm cages," *Front. Phys.* **19**, 332111 (2024).
- [40] J. Liu, Z.-F. Cai, T. Liu, and Z. Yang, "Reentrant non-Hermitian skin effect in coupled non-Hermitian and Hermitian chains with correlated disorder," [arXiv:2311.03777](https://arxiv.org/abs/2311.03777) (2023).
- [41] K. Kawabata, R. Sohal, and S. Ryu, "Lieb-Schultz-Mattis theorem in open quantum systems," *Phys. Rev. Lett.* **132**, 070402 (2024).

- [42] S. Manna and B. Roy, “Inner skin effects on non-Hermitian topological fractals,” *Communications Physics* **6**, 10 (2023).
- [43] Z.-F. Cai, T. Liu, and Z. Yang, “Non-Hermitian skin effect in periodically driven dissipative ultracold atoms,” *Phys. Rev. A* **109**, 063329 (2024).
- [44] M. Parto, C. Leefmans, J. Williams, F. Nori, and A. Marandi, “Non-Abelian effects in dissipative photonic topological lattices,” *Nat. Comm.* **14**, 1440 (2023).
- [45] W. Nie, T. Shi, Y.-x. Liu, and F. Nori, “Non-Hermitian waveguide cavity QED with tunable atomic mirrors,” *Phys. Rev. Lett.* **131**, 103602 (2023).
- [46] H.-Y. Wang, F. Song, and Z. Wang, “Amoeba formulation of non-Bloch band theory in arbitrary dimensions,” *Phys. Rev. X* **14**, 021011 (2024).
- [47] Y.-M. Hu, H.-Y. Wang, Z. Wang, and F. Song, “Geometric origin of non-Bloch \mathcal{PT} symmetry breaking,” *Phys. Rev. Lett.* **132**, 050402 (2024).
- [48] C. R. Leefmans, M. Parto, J. Williams, G. H. Y. Li, A. Dutt, F. Nori, and A. Marandi, “Topological temporally mode-locked laser,” *Nat. Phys.* **20**, 852 (2024).
- [49] Y. Ashida, S. Furukawa, and M. Ueda, “Parity-time-symmetric quantum critical phenomena,” *Nature Communications* **8** (2017), 10.1038/ncomms15791.
- [50] M. Nakagawa, N. Kawakami, and M. Ueda, “Non-Hermitian Kondo effect in ultracold alkaline-earth atoms,” *Phys. Rev. Lett.* **121**, 203001 (2018).
- [51] K. Yamamoto, M. Nakagawa, K. Adachi, K. Takasan, M. Ueda, and N. Kawakami, “Theory of Non-Hermitian fermionic superfluidity with a complex-valued interaction,” *Phys. Rev. Lett.* **123**, 123601 (2019).
- [52] M. Nakagawa, N. Tsuji, N. Kawakami, and M. Ueda, “Dynamical sign reversal of magnetic correlations in dissipative Hubbard models,” *Phys. Rev. Lett.* **124**, 147203 (2020).
- [53] T. Yoshida and Y. Hatsugai, “Correlation effects on non-Hermitian point-gap topology in zero dimension: Reduction of topological classification,” *Phys. Rev. B* **104**, 075106 (2021).
- [54] S.-B. Zhang, M. M. Denner, T. Bzdušek, M. A. Sentef, and T. Neupert, “Symmetry breaking and spectral structure of the interacting Hatano-Nelson model,” *Phys. Rev. B* **106**, L121102 (2022).
- [55] B. Dóra and C. P. Moca, “Full counting statistics in the many-body Hatano-Nelson model,” *Phys. Rev. B* **106**, 235125 (2022).
- [56] K. Kawabata, K. Shiozaki, and S. Ryu, “Many-body topology of non-Hermitian systems,” *Phys. Rev. B* **105**, 165137 (2022).
- [57] T. Liu, J. J. He, T. Yoshida, Z.-L. Xiang, and F. Nori, “Non-Hermitian topological Mott insulators in one-dimensional fermionic superlattices,” *Phys. Rev. B* **102**, 235151 (2020).
- [58] T. Yoshida and Y. Hatsugai, “Reduction of one-dimensional non-Hermitian point-gap topology by interactions,” *Phys. Rev. B* **106**, 205147 (2022).
- [59] R. Shen and C. H. Lee, “Non-Hermitian skin clusters from strong interactions,” *Commun. Phys.* **5**, 238 (2022).
- [60] W. N. Faugno and T. Ozawa, “Interaction-induced non-Hermitian topological phases from a dynamical gauge field,” *Phys. Rev. Lett.* **129**, 180401 (2022).
- [61] H. Li, H. Wu, W. Zheng, and W. Yi, “Many-body non-Hermitian skin effect under dynamic gauge coupling,” *Phys. Rev. Res.* **5**, 033173 (2023).
- [62] S. Longhi, “Spectral structure and doublon dissociation in the two-particle non-Hermitian Hubbard model,” *Ann. Phys.* **535**, 2300291 (2023).
- [63] L. Mao, Y. Hao, and L. Pan, “Non-Hermitian skin effect in a one-dimensional interacting bose gas,” *Phys. Rev. A* **107**, 043315 (2023).
- [64] Y. Qin and L. Li, “Occupation-dependent particle separation in one-dimensional non-Hermitian lattices,” *Phys. Rev. Lett.* **132**, 096501 (2024).
- [65] T. Yoshida, S.-B. Zhang, T. Neupert, and N. Kawakami, “Non-Hermitian Mott skin effect,” *Phys. Rev. Lett.* **133**, 076502 (2024).
- [66] Y. Qin, C. H. Lee, and L. Li, “Dynamical suppression of many-body non-Hermitian skin effect in anyonic systems,” arXiv:2405.1228 (2024).
- [67] P. Brighi and A. Nunnenkamp, “Non-reciprocal dynamics and non-Hermitian skin effect of repulsively bound pairs,” arXiv:2403.10449 (2024).
- [68] B. H. Kim, J.-H. Han, and M. J. Park, “Collective non-Hermitian skin effect: Point-gap topology and the doublon-holon excitations in non-reciprocal many-body systems,” *Commun. Phys.* **7**, 73 (2024).
- [69] S. E. Begg and R. Hanai, “Quantum criticality in open quantum spin chains with nonreciprocity,” *Phys. Rev. Lett.* **132**, 120401 (2024).
- [70] L. Mao, X. Yang, M.-J. Tao, H. Hu, and L. Pan, “Liouvillian skin effect in a one-dimensional open many-body quantum system with generalized boundary conditions,” *Phys. Rev. B* **110**, 045440 (2024).
- [71] L. Li, C. H. Lee, and J. Gong, “Topological switch for non-Hermitian skin effect in cold-atom systems with loss,” *Phys. Rev. Lett.* **124**, 250402 (2020).
- [72] Y. Yi and Z. Yang, “Non-Hermitian skin modes induced by on-site dissipations and chiral tunneling effect,” *Phys. Rev. Lett.* **125**, 186802 (2020).
- [73] Q. Liang, D. Xie, Z. Dong, H. Li, H. Li, B. Gadway, W. Yi, and B. Yan, “Dynamic signatures of non-Hermitian skin effect and topology in ultracold atoms,” *Phys. Rev. Lett.* **129**, 070401 (2022).
- [74] M. O. Scully and M. S. Zubairy, *Quantum Optics* (Cambridge University Press, 1997).
- [75] H. P. Breuer and F. Petruccione, *The Theory of Open Quantum Systems* (Oxford University Press, 2007).
- [76] D. A. Lidar, “Lecture notes on the theory of open quantum systems,” arXiv:1902.00967 (2020).
- [77] Y. Ashida, S. Furukawa, and M. Ueda, “Quantum critical behavior influenced by measurement backaction in ultracold gases,” *Phys. Rev. A* **94**, 053615 (2016).
- [78] See Supplemental Material for detailed derivations.
- [79] H. Cai, J. Liu, J. Wu, Y. He, S.-Y. Zhu, J.-X. Zhang, and D.-W. Wang, “Experimental observation of momentum-space chiral edge currents in room-temperature atoms,” *Phys. Rev. Lett.* **122**, 023601 (2019).
- [80] I. Tamm, “On the possible bound states of electrons on a crystal surface,” *Phys. Z. Soviet Union.* **1**, 733 (1932).
- [81] W. Shockley, “On the surface states associated with a periodic potential,” *Phys. Rev.* **56**, 317 (1939).
- [82] N. A. Olekhno, E. I. Kretov, A. A. Stepanenko, P. A. Ivanova, V. V. Yaroshenko, E. M. Puhtina, D. S. Filonov, B. Cappello, L. Matekovits, and M. A. Gorchakov, “Topological edge states of interacting photon pairs emulated in a topolectrical circuit,” *Nat. Commun.* **11**, 143901 (2020).

**SUPPLEMENTAL MATERIAL FOR “ DISSIPATION AND INTERACTION-CONTROLLED
NON-HERMITIAN SKIN EFFECTS”**

I. Effective Hamiltonian of Doublons

We consider the strong-interaction limit with $U \gg t, t'$ in the double-excitation subspace. In this case, the doublons are tightly bound, where their two-particle components reside on the same site. Moreover, the doublon states are energetically well-separated from two-particle scattering states. To derive the effective Hamiltonian $\hat{\mathcal{H}}_{\text{eff}}$ of doublons, we split the Hamiltonian $\hat{\mathcal{H}}_{\text{nH}}$ into its dominant term

$$\hat{\mathcal{H}}_0 = -(U + \frac{i\kappa}{2}) \sum_{j=1}^L \hat{a}_j^\dagger \hat{a}_j^\dagger \hat{a}_j \hat{a}_j - \frac{i}{2} \sum_{j=1}^L [\gamma - (-1)^j \delta] \hat{n}_j, \quad (\text{S1})$$

and a perturbation

$$\hat{V} = - \sum_{j=1}^L t \left(\hat{a}_{j+1}^\dagger \hat{a}_j + \text{H.c.} \right) - \sum_{j=1}^{L/2} \left(t' e^{-i\phi} \hat{a}_{2j+1}^\dagger \hat{a}_{2j-1} + t' e^{i\phi} \hat{a}_{2j+2}^\dagger \hat{a}_{2j} + \text{H.c.} \right). \quad (\text{S2})$$

In the strong-interaction limit, the tightly bound doublons mainly reside at the same site in the double-excitation subspace, where the double-occupied states read

$$|d_j\rangle \equiv \hat{a}_j^\dagger \hat{a}_j^\dagger |0\rangle = \hat{d}_j^\dagger |0\rangle. \quad (\text{S3})$$

Projecting $\hat{\mathcal{H}}_0$ onto $|d_j\rangle$ in the double-occupied states, for odd and even sites, we have

$$E_d^{\text{odd}} = -(2U + i\kappa) - i(\gamma + \delta), \quad E_d^{\text{even}} = -(2U + i\kappa) - i(\gamma - \delta). \quad (\text{S4})$$

In addition to the double-occupied states, the single-occupied states are written as

$$|s_{j'j}^1\rangle \equiv \hat{a}_{2j'-1}^\dagger \hat{a}_{2j-1}^\dagger |0\rangle \quad \text{for } j' \neq j, \quad |s_{j'j}^2\rangle \equiv \hat{a}_{2j'}^\dagger \hat{a}_{2j-1}^\dagger |0\rangle, \quad |s_{j'j}^3\rangle \equiv \hat{a}_{2j'}^\dagger \hat{a}_{2j}^\dagger |0\rangle \quad \text{for } j' \neq j. \quad (\text{S5})$$

Projecting $\hat{\mathcal{H}}_0$ onto these single-occupied states, we have

$$E_{s1} = -i(\gamma + \delta), \quad E_{s2} = -i\gamma, \quad E_{s3} = -i(\gamma - \delta). \quad (\text{S6})$$

Based on third-order quasidegenerate perturbation theory [S1-S3], the nonzero matrix elements of the effective Hamiltonian are given by

$$\begin{aligned} \langle d | \hat{\mathcal{H}}_{\text{eff}} | d' \rangle &= E_d \delta_{d,d'} + \langle d | \hat{V} | d' \rangle + \frac{1}{2} \sum_s \langle d | \hat{V} | s \rangle \langle s | \hat{V} | d' \rangle \times \left[\frac{1}{E_d - E_s} + \frac{1}{E_{d'} - E_s} \right] \\ &+ \frac{1}{2} \sum_{s s'} \langle d | \hat{V} | s \rangle \langle s | \hat{V} | s' \rangle \langle s' | \hat{V} | d' \rangle \times \left[\frac{1}{(E_d - E_s)(E_d - E_{s'})} + \frac{1}{(E_{d'} - E_s)(E_{d'} - E_{s'})} \right]. \end{aligned} \quad (\text{S7})$$

Inserting Eqs. (S1-S6) into Eq. (S7), we achieve the effective Hamiltonian of doublon bands

$$\begin{aligned} \hat{\mathcal{H}}_{\text{eff}} &= - \sum_{j=1}^{L-1} \left(t_R \hat{d}_{j+1}^\dagger \hat{d}_j + t_L \hat{d}_j^\dagger \hat{d}_{j+1} \right) - \sum_{j=1}^{L/2-2} \left(J_R^{\text{odd}} \hat{d}_{2j+1}^\dagger \hat{d}_{2j-1} + J_L^{\text{odd}} \hat{d}_{2j-1}^\dagger \hat{d}_{2j+1} \right) \\ &- \sum_{j=1}^{L/2-2} \left(J_R^{\text{even}} \hat{d}_{2j+2}^\dagger \hat{d}_{2j} + J_L^{\text{even}} \hat{d}_{2j}^\dagger \hat{d}_{2j+2} \right) + U_{\text{odd}} \sum_{j=1}^{L/2} \hat{d}_{2j-1}^\dagger \hat{d}_{2j-1} + U_{\text{even}} \sum_{j=1}^{L/2} \hat{d}_{2j}^\dagger \hat{d}_{2j}. \end{aligned} \quad (\text{S8})$$

In Eq. (S8), t_L and t_R are the nearest-neighbor hopping amplitudes of doublons, which are given by

$$\begin{aligned} t_L &= \langle d_j | \hat{\mathcal{H}}_{\text{eff}} | d_{j+1} \rangle \\ &= -t^2 \left(\frac{1}{E_d^{\text{odd}} - E_{s,2}} + \frac{1}{E_d^{\text{even}} - E_{s,2}} \right) + 2t^2 t' \cos \phi \left[\frac{1}{(E_d^{\text{odd}} - E_{s,2})^2} + \frac{1}{(E_d^{\text{even}} - E_{s,2})^2} \right] \\ &+ 2t^2 t' e^{i\phi} \left[\frac{1}{(E_d^{\text{odd}} - E_{s,1})(E_d^{\text{odd}} - E_{s,2})} + \frac{1}{(E_d^{\text{even}} - E_{s,1})(E_d^{\text{even}} - E_{s,2})} \right] \\ &+ 2t^2 t' e^{-i\phi} \left[\frac{1}{(E_d^{\text{odd}} - E_{s,3})(E_d^{\text{odd}} - E_{s,2})} + \frac{1}{(E_d^{\text{even}} - E_{s,3})(E_d^{\text{even}} - E_{s,2})} \right], \end{aligned} \quad (\text{S9})$$

$$\begin{aligned}
t_R &= \langle d_{j+1} | \hat{\mathcal{H}}_{\text{eff}} | d_j \rangle \\
&= -t^2 \left(\frac{1}{E_d^{\text{odd}} - E_{s,2}} + \frac{1}{E_d^{\text{even}} - E_{s,2}} \right) + 2t^2 t' \cos \phi \left[\frac{1}{(E_d^{\text{odd}} - E_{s,2})^2} + \frac{1}{(E_d^{\text{even}} - E_{s,2})^2} \right] \\
&\quad + 2t^2 t' e^{-i\phi} \left[\frac{1}{(E_d^{\text{odd}} - E_{s,1})(E_d^{\text{odd}} - E_{s,2})} + \frac{1}{(E_d^{\text{even}} - E_{s,1})(E_d^{\text{even}} - E_{s,2})} \right] \\
&\quad + 2t^2 t' e^{i\phi} \left[\frac{1}{(E_d^{\text{odd}} - E_{s,3})(E_d^{\text{odd}} - E_{s,2})} + \frac{1}{(E_d^{\text{even}} - E_{s,3})(E_d^{\text{even}} - E_{s,2})} \right]. \tag{S10}
\end{aligned}$$

The next-nearest-neighbor hopping amplitudes $J_{R/L}^{\text{odd}}$ and $J_{R/L}^{\text{even}}$ of doublons are derived as

$$J_R^{\text{odd}} = \langle d_{2j+1} | \hat{\mathcal{H}}_{\text{eff}} | d_{2j-1} \rangle = -\frac{2t'^2 e^{-2i\phi}}{E_d^{\text{odd}} - E_{s,1}} + \frac{2t^2 t' e^{-i\phi}}{(E_d^{\text{odd}} - E_{s,2})^2} + \frac{4t^2 t' e^{-i\phi}}{(E_d^{\text{odd}} - E_{s,1})(E_d^{\text{odd}} - E_{s,2})}, \tag{S11}$$

$$J_L^{\text{odd}} = \langle d_{2j-1} | \hat{\mathcal{H}}_{\text{eff}} | d_{2j+1} \rangle = -\frac{2t'^2 e^{2i\phi}}{E_d^{\text{odd}} - E_{s,1}} + \frac{2t^2 t' e^{i\phi}}{(E_d^{\text{odd}} - E_{s,2})^2} + \frac{4t^2 t' e^{i\phi}}{(E_d^{\text{odd}} - E_{s,1})(E_d^{\text{odd}} - E_{s,2})}, \tag{S12}$$

$$J_R^{\text{even}} = \langle d_{2j+2} | \hat{\mathcal{H}}_{\text{eff}} | d_{2j} \rangle = -\frac{2t'^2 e^{2i\phi}}{E_d^{\text{even}} - E_{s,3}} + \frac{2t^2 t' e^{i\phi}}{(E_d^{\text{even}} - E_{s,2})^2} + \frac{4t^2 t' e^{i\phi}}{(E_d^{\text{even}} - E_{s,3})(E_d^{\text{even}} - E_{s,2})}, \tag{S13}$$

$$J_L^{\text{even}} = \langle d_{2j} | \hat{\mathcal{H}}_{\text{eff}} | d_{2j+2} \rangle = -\frac{2t'^2 e^{-2i\phi}}{E_d^{\text{even}} - E_{s,3}} + \frac{2t^2 t' e^{-i\phi}}{(E_d^{\text{even}} - E_{s,2})^2} + \frac{4t^2 t' e^{-i\phi}}{(E_d^{\text{even}} - E_{s,3})(E_d^{\text{even}} - E_{s,2})}. \tag{S14}$$

The onsite potentials U_{odd} and U_{even} for odd and even sites are given by

$$U_{\text{odd}} = \langle d_{2j-1} | \hat{\mathcal{H}}_{\text{eff}} | d_{2j-1} \rangle = E_d^{\text{odd}} + \frac{4t^2}{E_d^{\text{odd}} - E_{s,2}} + \frac{4t'^2}{E_d^{\text{odd}} - E_{s,1}} - \frac{4t^2 t' \cos \phi}{(E_d^{\text{odd}} - E_{s,2})^2} - \frac{8t^2 t' \cos \phi}{(E_d^{\text{odd}} - E_{s,1})(E_d^{\text{odd}} - E_{s,2})}, \tag{S15}$$

$$U_{\text{even}} = \langle d_{2j} | \hat{\mathcal{H}}_{\text{eff}} | d_{2j} \rangle = E_d^{\text{even}} + \frac{4t^2}{E_d^{\text{even}} - E_{s,2}} + \frac{4t'^2}{E_d^{\text{even}} - E_{s,3}} - \frac{4t^2 t' \cos \phi}{(E_d^{\text{even}} - E_{s,2})^2} - \frac{8t^2 t' \cos \phi}{(E_d^{\text{even}} - E_{s,3})(E_d^{\text{even}} - E_{s,2})}. \tag{S16}$$

According to Eq. (S7), under OBCs, the nearest-neighbor hopping amplitudes and onsite potentials involving boundary sites should be modified, and they are given by

$$\begin{aligned}
t_L &= \langle d_1 | \hat{\mathcal{H}}_{\text{eff}} | d_2 \rangle \\
&= -t^2 \left(\frac{1}{E_d^{\text{odd}} - E_{s,2}} + \frac{1}{E_d^{\text{even}} - E_{s,2}} \right) + t^2 t' e^{i\phi} \left[\frac{1}{(E_d^{\text{odd}} - E_{s,2})^2} + \frac{1}{(E_d^{\text{even}} - E_{s,2})^2} \right] \\
&\quad + 2t^2 t' e^{i\phi} \left[\frac{1}{(E_d^{\text{odd}} - E_{s,1})(E_d^{\text{odd}} - E_{s,2})} + \frac{1}{(E_d^{\text{even}} - E_{s,1})(E_d^{\text{even}} - E_{s,2})} \right], \quad \text{for } j = 1, \tag{S17}
\end{aligned}$$

$$\begin{aligned}
t_R &= \langle d_2 | \hat{\mathcal{H}}_{\text{eff}} | d_1 \rangle \\
&= -t^2 \left(\frac{1}{E_d^{\text{odd}} - E_{s,2}} + \frac{1}{E_d^{\text{even}} - E_{s,2}} \right) + t^2 t' e^{-i\phi} \left[\frac{1}{(E_d^{\text{odd}} - E_{s,2})^2} + \frac{1}{(E_d^{\text{even}} - E_{s,2})^2} \right] \\
&\quad + 2t^2 t' e^{-i\phi} \left[\frac{1}{(E_d^{\text{odd}} - E_{s,1})(E_d^{\text{odd}} - E_{s,2})} + \frac{1}{(E_d^{\text{even}} - E_{s,1})(E_d^{\text{even}} - E_{s,2})} \right], \quad \text{for } j = 1, \tag{S18}
\end{aligned}$$

$$\begin{aligned}
t_L &= \langle d_{L-1} | \hat{\mathcal{H}}_{\text{eff}} | d_L \rangle \\
&= -t^2 \left(\frac{1}{E_d^{\text{odd}} - E_{s,2}} + \frac{1}{E_d^{\text{even}} - E_{s,2}} \right) + t^2 t' e^{-i\phi} \left[\frac{1}{(E_d^{\text{odd}} - E_{s,2})^2} + \frac{1}{(E_d^{\text{even}} - E_{s,2})^2} \right] \\
&\quad + 2t^2 t' e^{-i\phi} \left[\frac{1}{(E_d^{\text{odd}} - E_{s,3})(E_d^{\text{odd}} - E_{s,2})} + \frac{1}{(E_d^{\text{even}} - E_{s,3})(E_d^{\text{even}} - E_{s,2})} \right], \quad \text{for } j = L - 1, \tag{S19}
\end{aligned}$$

$$\begin{aligned}
t_R &= \langle d_L | \hat{\mathcal{H}}_{\text{eff}} | d_{L-1} \rangle \\
&= -t^2 \left(\frac{1}{E_d^{\text{odd}} - E_{s,2}} + \frac{1}{E_d^{\text{even}} - E_{s,2}} \right) + t^2 t' e^{i\phi} \left[\frac{1}{(E_d^{\text{odd}} - E_{s,2})^2} + \frac{1}{(E_d^{\text{even}} - E_{s,2})^2} \right] \\
&\quad + 2t^2 t' e^{i\phi} \left[\frac{1}{(E_d^{\text{odd}} - E_{s,3})(E_d^{\text{odd}} - E_{s,2})} + \frac{1}{(E_d^{\text{even}} - E_{s,3})(E_d^{\text{even}} - E_{s,2})} \right], \quad \text{for } j = L-1, \tag{S20}
\end{aligned}$$

$$\begin{aligned}
U_{\text{odd}} &\equiv \langle d_1 | \hat{\mathcal{H}}_{\text{eff}} | d_1 \rangle \\
&= E_d^{\text{odd}} + \frac{2t^2}{E_d^{\text{odd}} - E_{s,2}} + \frac{2t'^2}{E_d^{\text{odd}} - E_{s,1}} - \frac{4t^2 t' \cos \phi}{(E_d^{\text{odd}} - E_{s,1})(E_d^{\text{odd}} - E_{s,2})}, \quad \text{for } j = 1, \tag{S21}
\end{aligned}$$

$$\begin{aligned}
U_{\text{even}} &\equiv \langle d_2 | \hat{\mathcal{H}}_{\text{eff}} | d_2 \rangle \\
&= E_d^{\text{even}} + \frac{4t^2}{E_d^{\text{even}} - E_{s,2}} + \frac{2t'^2}{E_d^{\text{even}} - E_{s,3}} - \frac{4t^2 t' \cos \phi}{(E_d^{\text{even}} - E_{s,2})^2} - \frac{4t^2 t' \cos \phi}{(E_d^{\text{even}} - E_{s,3})(E_d^{\text{even}} - E_{s,2})}, \quad \text{for } j = 2, \tag{S22}
\end{aligned}$$

$$\begin{aligned}
U_{\text{odd}} &\equiv \langle d_{L-1} | \hat{\mathcal{H}}_{\text{eff}} | d_{L-1} \rangle \\
&= E_d^{\text{odd}} + \frac{4t^2}{E_d^{\text{odd}} - E_{s,2}} + \frac{2t'^2}{E_d^{\text{odd}} - E_{s,1}} - \frac{4t^2 t' \cos \phi}{(E_d^{\text{odd}} - E_{s,2})^2} - \frac{4t^2 t' \cos \phi}{(E_d^{\text{odd}} - E_{s,1})(E_d^{\text{odd}} - E_{s,2})}, \quad \text{for } j = L-1, \tag{S23}
\end{aligned}$$

$$\begin{aligned}
U_{\text{even}} &\equiv \langle d_L | \hat{\mathcal{H}}_{\text{eff}} | d_L \rangle \\
&= E_d^{\text{even}} + \frac{2t^2}{E_d^{\text{even}} - E_{s,2}} + \frac{2t'^2}{E_d^{\text{even}} - E_{s,3}} - \frac{4t^2 t' \cos \phi}{(E_d^{\text{even}} - E_{s,2})^2}, \quad \text{for } j = L. \tag{S24}
\end{aligned}$$

For large U , we can neglect the higher-order terms in Eqs. (S9), (S10) and (S15)-(S24). Then, we can further simplify the effective Hamiltonian in Eqs. (S8)-(S24) as

$$\begin{aligned}
\hat{\mathcal{H}}_{\text{eff}} &= -t_0 \sum_{j=1}^{L-1} \left(\hat{d}_{j+1}^\dagger \hat{d}_j + \hat{d}_j^\dagger \hat{d}_{j+1} \right) - \sum_{j=1}^{L/2-2} \left(J_{1,R} \hat{d}_{2j+1}^\dagger \hat{d}_{2j-1} + J_{1,L} \hat{d}_{2j-1}^\dagger \hat{d}_{2j+1} \right) \\
&\quad - \sum_{j=1}^{L/2-2} \left(J_{2,R} \hat{d}_{2j+2}^\dagger \hat{d}_{2j} + J_{2,L} \hat{d}_{2j}^\dagger \hat{d}_{2j+2} \right) + U_1 \sum_{j=1}^{L/2} \hat{d}_{2j-1}^\dagger \hat{d}_{2j-1} + U_2 \sum_{j=1}^{L/2} \hat{d}_{2j}^\dagger \hat{d}_{2j}, \tag{S25}
\end{aligned}$$

where

$$t_0 = \left[\frac{2U}{4U^2 + (\kappa + \delta)^2} + \frac{2U}{4U^2 + (\kappa - \delta)^2} \right] t^2 - i \left(\frac{\kappa + \delta}{4U^2 + (\kappa + \delta)^2} + \frac{\kappa - \delta}{4U^2 + (\kappa - \delta)^2} \right) t^2, \tag{S26}$$

$$J_{1,R} = \left[\frac{2t^2 t'}{(2U + i\kappa + i\delta)^2} + \frac{4t^2 t'}{(2U + i\kappa)(2U + i\kappa + i\delta)} \right] e^{-i\phi} + \frac{2t'^2}{2U + i\kappa} e^{-2i\phi}, \tag{S27}$$

$$J_{1,L} = \left[\frac{2t^2 t'}{(2U + i\kappa + i\delta)^2} + \frac{4t^2 t'}{(2U + i\kappa)(2U + i\kappa + i\delta)} \right] e^{i\phi} + \frac{2t'^2}{2U + i\kappa} e^{2i\phi}, \tag{S28}$$

$$J_{2,R} = \left[\frac{2t^2 t'}{(2U + i\kappa - i\delta)^2} + \frac{4t^2 t'}{(2U + i\kappa)(2U + i\kappa - i\delta)} \right] e^{i\phi} + \frac{2t'^2}{2U + i\kappa} e^{2i\phi}, \tag{S29}$$

$$J_{2,L} = \left[\frac{2t^2 t'}{(2U + i\kappa - i\delta)^2} + \frac{4t^2 t'}{(2U + i\kappa)(2U + i\kappa - i\delta)} \right] e^{-i\phi} + \frac{2t'^2}{2U + i\kappa} e^{-2i\phi}, \tag{S30}$$

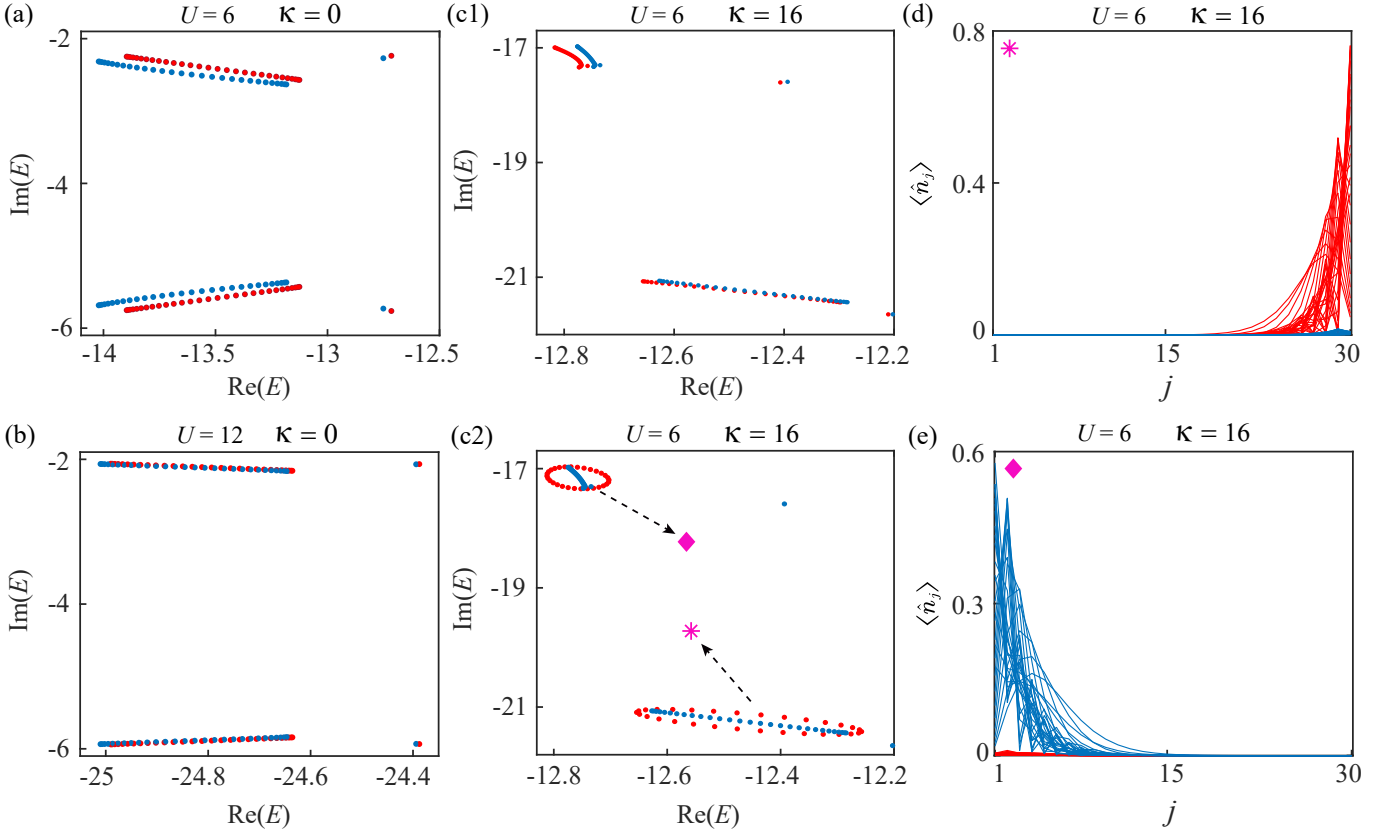


FIG. S1. (a,b,c1) Complex eigenenergies of doublons calculated using $\hat{\mathcal{H}}_{\text{nH}}$ (red dots) and the effective Hamiltonian $\hat{\mathcal{H}}_{\text{eff}}$ (blue dots) in the strong-interaction limit under OBCs, where doublon spectra are well captured by the effective Hamiltonian $\hat{\mathcal{H}}_{\text{eff}}$ for the large U . (c2) Doublon bands of $\hat{\mathcal{H}}_{\text{eff}}$ under OBCs (blue dots) and PBCs (red dots), where the magenta star and diamond denote the two branches of the doublon bands. The corresponding particle densities $\langle \hat{n}_j \rangle$ using $\hat{\mathcal{H}}_{\text{eff}}$ are shown in (d) and (e), where the red (blue) curves indicate the state distributions at the odd (even) sites. Other parameters are: $\phi = \pi/2$, $t = 2$, $t' = 1$, $\gamma = 4$, $\delta = 2$, and $L = 60$.

$$U_1 = - \left[2U + \frac{8Ut^2}{4U^2 + (\kappa + \delta)^2} + \frac{8Ut'^2}{4U^2 + \kappa^2} \right] + i \left[\frac{4(\kappa + \delta)t^2}{4U^2 + (\kappa + \delta)^2} + \frac{4\kappa t'^2}{4U^2 + \kappa^2} - \kappa - \gamma - \delta \right], \quad (\text{S31})$$

$$U_2 = - \left[2U + \frac{8Ut^2}{4U^2 + (\kappa - \delta)^2} + \frac{8Ut'^2}{4U^2 + \kappa^2} \right] + i \left[\frac{4(\kappa - \delta)t^2}{4U^2 + (\kappa - \delta)^2} + \frac{4\kappa t'^2}{4U^2 + \kappa^2} - \kappa - \gamma + \delta \right]. \quad (\text{S32})$$

We plot the complex eigenenergies of doublon bands calculated using $\hat{\mathcal{H}}_{\text{nH}}$ (red dots) and the effective Hamiltonian $\hat{\mathcal{H}}_{\text{eff}}$ (blue dots) in the strong-interaction limit under OBCs, as shown in Fig. S1(a,b,c1). The effective Hamiltonian $\hat{\mathcal{H}}_{\text{eff}}$ exhibits a well approximation to the exact results from $\hat{\mathcal{H}}_{\text{nH}}$ for the large U . The site-resolved particle density $\langle \hat{n}_j \rangle$ of doublons, corresponding to the existence of both single-particle and two-particle losses [see zoom-in spectrum in Fig. S1(c2)], is shown in Fig. S1(d,f), where state distributions are well captured by the effective Hamiltonian.

According to the effective Hamiltonian in Eq. (S25), the magnetic flux threading through each triangular plaquette and the imbalanced onsite potential $U(\pm\delta)$ in odd and even sites are renormalized. Most remarkably, along each leg of the zigzag lattice, the virtual second-order hopping process of the particle pairs contributes to an effective phase 2ϕ , and third-order process contributes to ϕ according to Eqs. (S7) and (S11)-(S14). Therefore, the effective next-nearest-neighbor hopping of doublons becomes nonreciprocal, i.e., $|J_{i,\text{R}}| \neq |J_{i,\text{L}}|$ ($i = 1, 2$), due to the interplay of two-particle dissipation and magnetic flux. Moreover, the nonreciprocal-hopping direction can be different between its two legs, determined by the interaction strength U , two-particle loss κ , and imbalanced single-particle loss δ . These indicates that the skin-mode localization direction of doublons is determined by the competition between the effective nonreciprocal hopping, induced by the two-particle dissipation, the magnetic flux, and the directional hopping due to the interplay of magnetic-flux-induced chiral transport and imbalanced loss along two legs. This contrasts with the

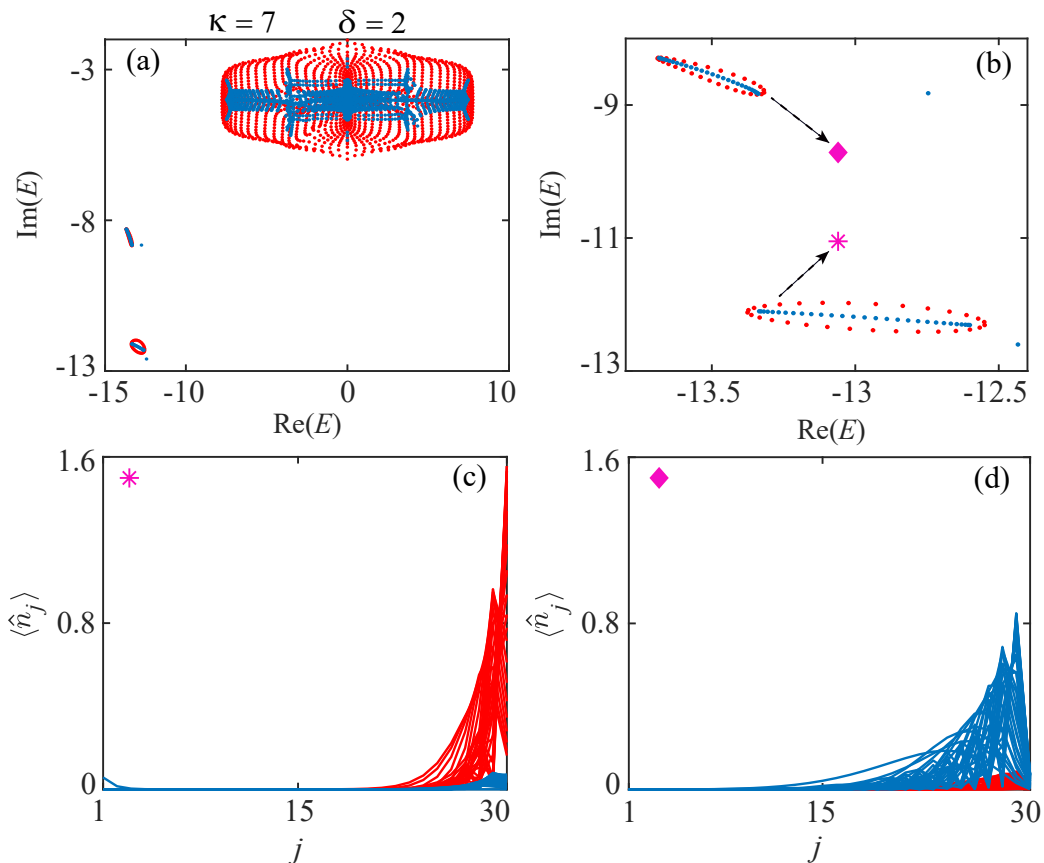


FIG. S2. (a) Complex eigenenergies of $\hat{\mathcal{H}}_{\text{nH}}$ under OBCs (blue dots) and PBCs (red dots) in the presence of the single-particle dissipation for $\kappa = 7$. The discrete doubton bands are well separated from the continuum of scattering states. The zoom-in view of the two doubton bands on the far left of (a) is shown in (b), where the magenta star and diamond denote the two branches of the doubton bands. The corresponding particle densities $\langle \hat{n}_j \rangle$ are shown in (c) and (d) under OBCs, where the red (blue) curves indicate the state distributions at the odd (even) sites. Other parameters are: $U = 6$, $t = 2$, $t' = 1$, $\gamma = 4$, $\delta = 2$, and $L = 60$.

single-particle case, where the NHSE results from the interplay of the magnetic-flux induced chiral transport and the imbalanced onsite loss along two legs of the zigzag lattice structure.

By fixing $U = 6$ and $\delta = 2$, we have $|J_{1,R}| > |J_{1,L}|$ and $|J_{2,R}| < |J_{2,L}|$ for $\kappa > \delta$. If the two-particle dissipation κ is comparable with the interaction strength U , states from two doubton bands are localized at the right boundary, which is attributed to the interplay of the renormalized magnetic flux and the effective imbalanced loss of doublons in spite of slightly stronger hopping of doublons towards the left boundary along the upper leg. In Fig. S2, we plot the complex eigenenergies of $\hat{\mathcal{H}}_{\text{nH}}$ under OBCs (blue dots) and PBCs (red dots), and corresponding density distribution of the doubton bands, where the doublons are localized at the right boundary for $\kappa = 7$.

As discussed in the main text, by fixing $U = 6$ and $\delta = 2$, when the two-particle dissipation κ becomes much larger than the interaction strength U , the localization direction of the states from one of doubton bands is reversed due to the competition between the effective nonreciprocal hopping, induced by the two-particle dissipation and magnetic flux, and the directional hopping due to the interplay of magnetic-flux induced chiral transport and imbalanced loss along two legs. Furthermore, if δ is increased and becomes comparable with κ , we have $|J_{1,R}| > |J_{1,L}|$ and $|J_{2,R}| > |J_{2,L}|$. It causes the once more reversal of the NHSE along the even sites, as shown in Fig. S3.

II. Two-particle Tamm-Shockley Edge States

With open boundary conditions, the renormalized onsite potentials in the boundary and bulk sites are different. Inside the bulk sites, the onsite potentials are given in Eqs. (S31) and (S32). At the boundary sites, the onsite

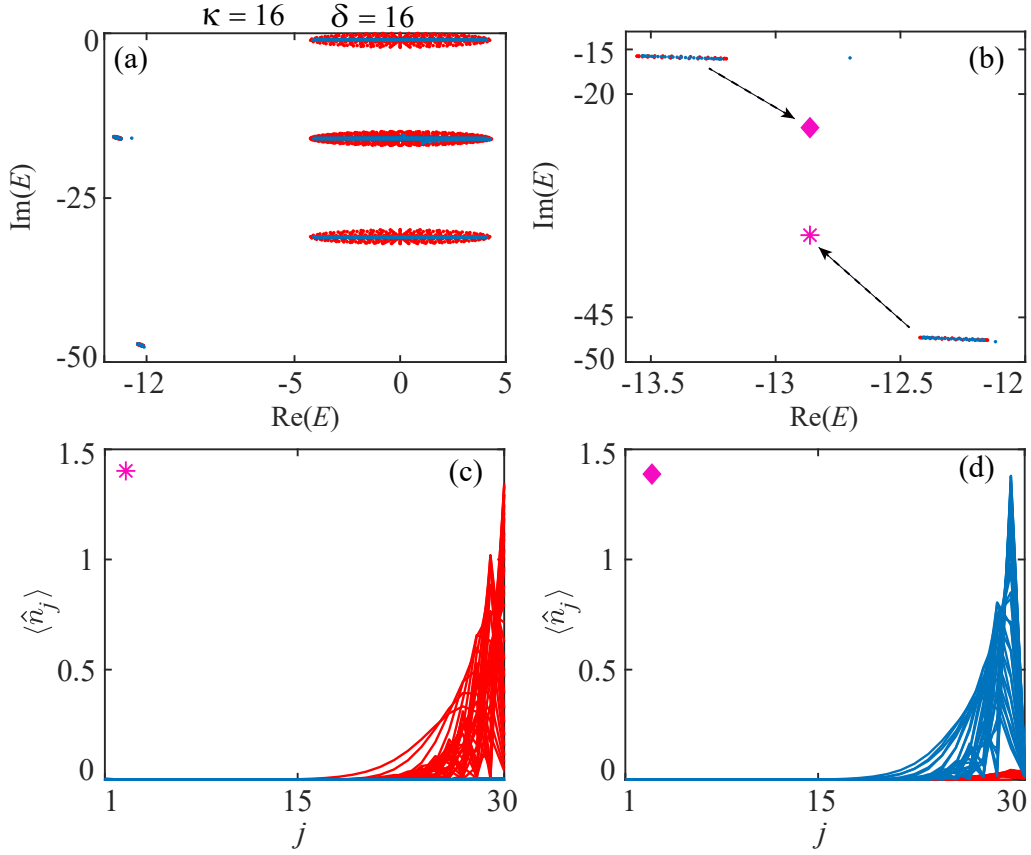


FIG. S3. (a) Complex eigenenergies of $\hat{\mathcal{H}}_{\text{NH}}$ under OBCs (blue dots) and PBCs (red dots) in the presence of the single-particle dissipation for $\kappa = \delta = 16$. The discrete doubloon bands are well separated from the continuum of scattering states. The zoom-in view of the two doubloon bands on the far left of (a) is shown in (b), where the magenta star and diamond denote the two branches of the doubloon bands. The corresponding particle densities $\langle \hat{n}_j \rangle$ are shown in (c) and (d) under OBCs, where the red (blue) curves indicate the state distributions at the odd (even) sites. Other parameters are: $U = 6$, $t = 2$, $t' = 1$, $\gamma = 4$, and $L = 60$.

potentials are derived as

$$U_{\text{edge}} = - \left(2U + \frac{4Ut^2}{4U^2 + (\kappa + \delta)^2} + \frac{4U(t')^2}{4U^2 + \kappa^2} \right) + i \left[\frac{2(\kappa + \delta)t^2}{4U^2 + (\kappa + \delta)^2} + \frac{2\kappa(t')^2}{4U^2 + \kappa^2} - \kappa - \gamma - \delta \right], \quad \text{for } j = 1, \quad (\text{S33})$$

$$U_{\text{edge}} = - \left(2U + \frac{8Ut^2}{4U^2 + (\kappa - \delta)^2} + \frac{4U(t')^2}{4U^2 + \kappa^2} \right) + i \left[\frac{4(\kappa - \delta)t^2}{4U^2 + (\kappa - \delta)^2} + \frac{2\kappa(t')^2}{4U^2 + \kappa^2} - \kappa - \gamma + \delta \right], \quad \text{for } j = 2, \quad (\text{S34})$$

$$U_{\text{edge}} = - \left(2U + \frac{8Ut^2}{4U^2 + (\kappa + \delta)^2} + \frac{4U(t')^2}{4U^2 + \kappa^2} \right) + i \left[\frac{4(\kappa + \delta)t^2}{4U^2 + (\kappa + \delta)^2} + \frac{2\kappa(t')^2}{4U^2 + \kappa^2} - \kappa - \gamma - \delta \right], \quad \text{for } j = L - 1, \quad (\text{S35})$$

$$U_{\text{edge}} = - \left(2U + \frac{4Ut^2}{4U^2 + (\kappa - \delta)^2} + \frac{4U(t')^2}{4U^2 + \kappa^2} \right) + i \left[\frac{2(\kappa - \delta)t^2}{4U^2 + (\kappa - \delta)^2} + \frac{2\kappa(t')^2}{4U^2 + \kappa^2} - \kappa - \gamma + \delta \right], \quad \text{for } j = L, \quad (\text{S36})$$

where L is an even number. Due to the different onsite potentials between boundary and bulk sites (magenta diamond and star), two isolated states of doublons, lying outside the point gaps, are localized at either the left or right boundaries [see Fig. S4]. There are called two-particle Tamm-Shockley states [S4, S5], which have no topological origin.

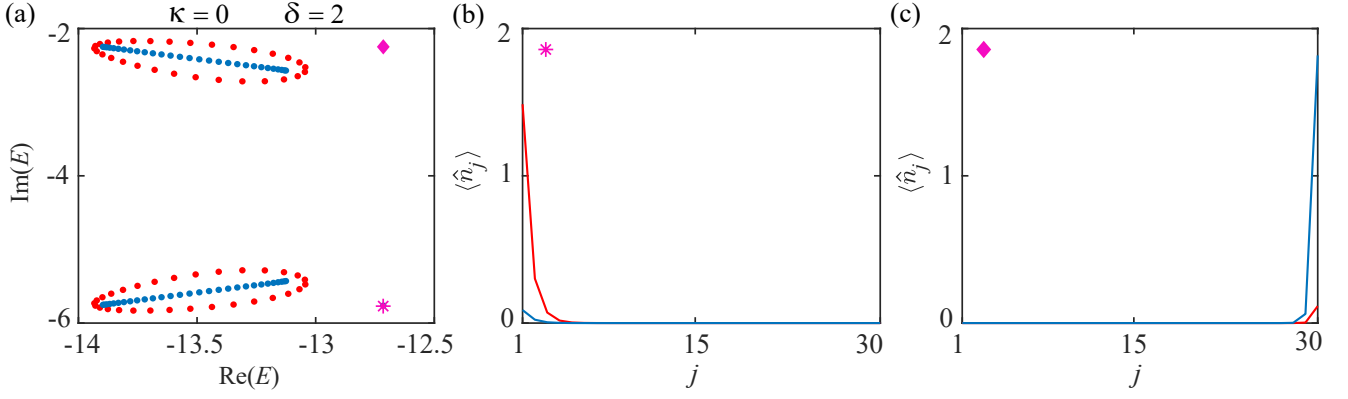


FIG. S4. (a) Complex eigenenergies of doublons under OBCs (blue dots) and PBCs (red dots), where the magenta star and diamond denote Tamm-Shockley states under OBCs. The corresponding particle densities $\langle \hat{n}_j \rangle$ are shown in (b) and (c) under OBCs, where the red (blue) curves indicate state distributions at the odd (even) sites. Other parameters are: $U = 6$, $t = 2$, $t' = 1$, $\kappa = 0$, $\gamma = 4$, $\delta = 2$, and $L = 60$.

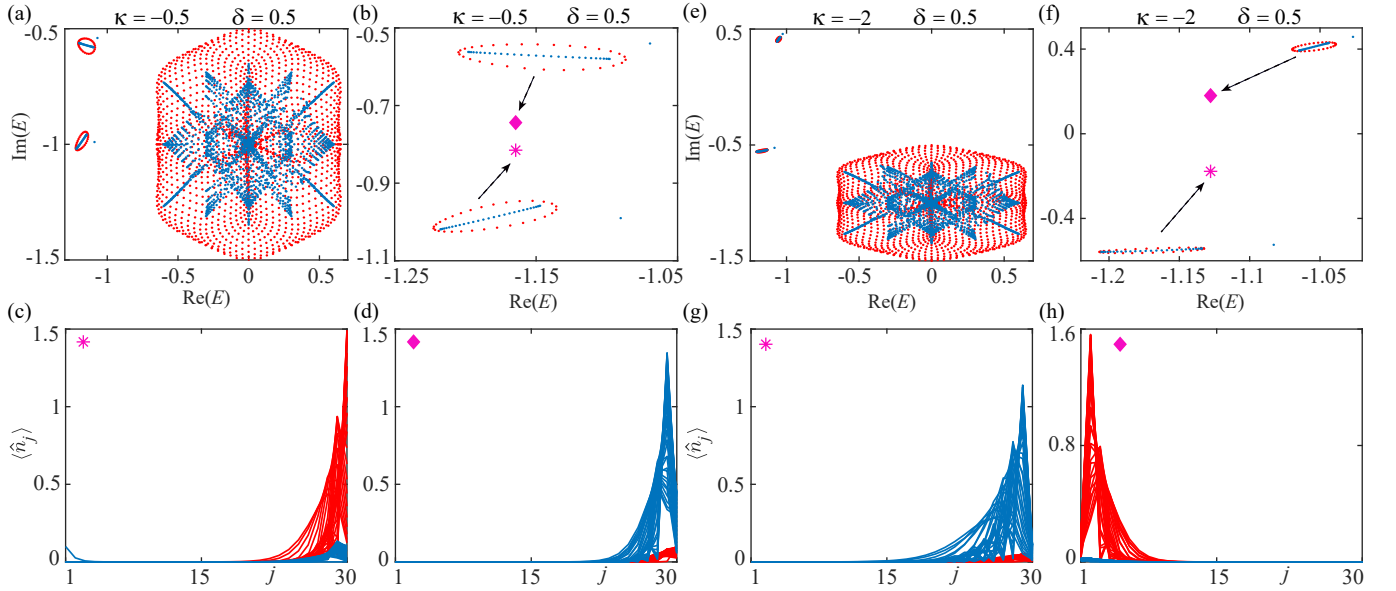


FIG. S5. Complex eigenenergies of $\hat{\mathcal{H}}_{\text{NHG}}$ under OBCs (blue dots) and PBCs (red dots) subjected to the two-particle gain (a) for $\kappa = -0.5$ and (e) for $\kappa = -2$. The zoom-in view of the two doublon bands on the far left of (a) and (e) is shown in (b) and (f), respectively, where the magenta star and diamond denote the two branches of the doublon bands. The corresponding particle densities $\langle \hat{n}_j \rangle$ are shown in (c,d) and (g,h) under OBCs, where red (blue) curves indicate the state distributions at the odd (even) sites. Other parameters are: $U = 0.5$, $t = 0.2$, $t' = 0.1$, $\gamma = 1$, $\delta = 0.5$, and $L = 60$.

III. Complex Spectrum for Two-particle Gain

In the main text, we discuss the reversal of the NHSE induced by the two-particle dissipation. In this section, we reveal that the two-particle gain along one leg can also induce a reversal of the NHSE, where the hidden physical mechanism is not trivial. For the two-particle gain introduced by the incoherent two-particle pumping along the odd sites, the effective non-Hermitian Hamiltonian of the system is written as

$$\hat{\mathcal{H}}_{\text{NHG}} = \hat{\mathcal{H}} - i \frac{\kappa}{2} \sum_{j=1}^{L/2} \hat{a}_{2j-1}^\dagger \hat{a}_{2j-1}^\dagger \hat{a}_{2j-1} \hat{a}_{2j-1} - \frac{i}{2} \sum_{j=1}^L [\gamma - (-1)^j \delta] \hat{n}_j, \quad (\text{S37})$$

where $\kappa < 0$.

In Fig. S5, we plot the complex eigenenergies of $\hat{\mathcal{H}}_{\text{NHG}}$ under OBCs (blue dots) and PBCs (red dots) subject to the two-particle gain introduced at the odd sites. The eigenenergies for OBCs are enclosed by the loop of the point

gap [see Fig. S5(a,b,e,f)], indicating the appearance of NHSE [see Fig. S5(c,d,g,h)]. To be specific, for the small two-particle gain, with $\kappa = -0.5$, the skin-doublon states are localized at the right boundary due to the larger total loss at the odd sites in Eqs. (S31) and (S32) and larger hopping strength towards the right sides with $|J_{i,R}| > |J_{i,L}|$ ($i = 1, 2$) in Eqs. (S27)-(S30) for $\gamma = 2\delta = 1$, as shown in Fig. S5(c,d). Note that the skin-mode localization at the right boundary for small $|\kappa|$ is mainly attributed to the interplay of the magnetic-flux induced chiral transport and the larger onsite loss along the odd sites.

When the two-particle gain $|\kappa|$ becomes much larger than the interaction strength U , the effective loss (it is equivalent to add a large background loss) at the odd sites becomes smaller than that at the even sites. The interplay of the magnetic-flux induced chiral transport and the imbalanced onsite loss should cause all the doublon states localized at the left boundary. However, not all the doublon states are localized towards the left boundary, and the only states from the doublon band with the larger imaginary parts of the eigenenergies are localized at the left boundary [see Fig. S5(h)], where these mainly occupy the odd sites. The states from the other doublon band are still unexpectedly localized at the right boundary along the even sites [see Fig. S5(g)]. The reason for this is that the effective hopping of doublons has a stronger hopping towards right side than left side, i.e., $|J_{2,R}| \gg |J_{2,L}|$ along the even sites. while, it is $|J_{1,L}| > |J_{1,R}|$ along the odd sites. For a strong two-particle gain, the skin-mode localization direction of doublons is determined by the competition between the effective nonreciprocal hopping, induced by the two-particle gain and the magnetic flux, and the directional hopping due to the interplay of the magnetic-flux induced chiral transport and imbalanced gain along the two legs.

* These authors contributed equally

† E-mail: liutao0716@scut.edu.cn

[S1] G. L. Bir and G. Pikus, *Symmetry and Strain-Induced Effects in Semiconductors* (Keter, Jerusalem, 1974).

[S2] C. Cohen-Tannoudji, J. Dupont-Roc, and G. Grynberg, *Atom-Photon Interactions* (John Wiley and Sons, 1998).

[S3] G. Salerno, M. Di Liberto, C. Menotti, and I. Carusotto, “Topological two-body bound states in the interacting Haldane model,” *Phys. Rev. A* **97**, 013637 (2018).

[S4] I. Tamm, *Phys. Z. Soviet Union.* **1**, 733 (1932).

[S5] W. Shockley, “On the surface states associated with a periodic potential,” *Phys. Rev.* **56**, 317 (1939).